DUAL-CODE SOLUTION PROCEDURE FOR EQUILIBRIUM HYPERSONIC AXISYMMETRIC TRANSITIONAL/TURBULENT FLOWS

Kazem Hejranfar[1], Vahid Esfahanian[2] and Ramin Kamali Moghadam[3]
[1,3]**Aerospace Engineering Department, Sharif University of Technology, Tehran, Iran**
[2] **Mechanical Engineering Department, University of Tehran, Tehran, Iran**

Keywords: *Hypersonic Equilibrium Flows, Blunt-Body, Transitional/Turbulent Flows*

Abstract

An appropriate combination of the thin-layer Navier-Stokes (TLNS) and parabolized Navier-Stokes (PNS) solvers is used to accurately and efficiently compute hypersonic transitional/turbulent flowfields of perfect gas and equilibrium air around blunt-body configurations. The TLNS equations are solved in the nose region to provide the initial data plane needed for the solution of the PNS equations. Then the PNS equations are employed to efficiently compute the flowfield for the afterbody region by using a space marching technique. Both the TLNS and the PNS equations are numerically solved by using the implicit non-iterative finite-difference algorithm of Beam and Warming. A shock fitting procedure is used in both the TLNS and PNS codes to obtain accurate solution in the vicinity of the shock. For turbulent flow simulations, both the Cebeci-Smith (CS) and the Baldwin-Lomax (BL) turbulence models are analyzed with the present technique for the case of long slender blunt bodies. The Baldwin-Lomax turbulence model, which does not need the determination of the edge of the boundary layer, is modified in the present work for pressure-gradient effects to accurately calculate flowfield characteristics. Detailed comparisons are made with other numerical and experimental results to assess the accuracy and efficiency of the present solution procedure for computing hypersonic flow over long slender blunt bodies. The results of these computations are found to be in good agreement with available data. The effects of real gas on the flowfield characteristics are also studied.

1 Introduction

Hypersonic flows are very important for design of high speed aircraft and reentry vehicles and some aerodynamic problems must be considered. Most of these problems arise because of extremely high flight altitudes, high flight velocities and high temperatures. The high temperatures and high convective velocities create an environment where real gas effects can be significant. The accurate and efficient design of thermal protection systems, as well as propulsion systems for such vehicles will require accurate information of various aerothermodynamics environments. Since the aerothermodynamics environment for these flight conditions (high speeds and high temperatures) is extremely difficult to simulate in ground-based or flight experiments, the design process for these vehicles will heavily based on computational methods to define the aerothermodynamics environment during re-entry.

Two common computational approaches for obtaining accurate aerothermodynamics predictions of these vehicles are to use the thin-layer Navier-Stokes (TLNS) equations or the parabolized Navier-Stokes (PNS) equations. The numerical computations of hypersonic viscous flows using the TLNS equations especially for long slender blunt bodies are very time consuming and require very high storage and computer speed. Therefore, they are not

well suited for various parametric studies needed for design and analysis processes.

An appropriate scheme for the computation of high speed flows over slender-body supersonic/hypersonic geometries is to use the PNS equations. The PNS equations are parabolic-like with respect to the streamwise direction; hence the PNS scheme can realize appreciable decreases in both computational time and memory requirements relative to the TLNS scheme. The main difficulty in applying the PNS approach over blunt-body configurations is that the PNS equations cannot solve the subsonic flowfield in the blunted nose, and therefore the TLNS equations must be used.

An alternative is to utilize a dual-code solution procedure, that is, the use of a TLNS solver in the nose region and using a PNS solver for the afterbody region. This strategy can efficiently be implemented for computations of hypersonic blunt-body configurations [1,2,3].

Wood and Eberhardt [1] and Wood et al. [2] used such a solution strategy for computation of hypersonic flowfields over blunt-body geometries using two well-established TLNS and PNS codes, LAURA [4] and UPS [5]. These two codes were based on finite volume, shock capturing algorithms. The application of the dual-code solution procedure was shown for the solution of perfect gas, equilibrium and chemically reacting hypersonic laminar flows about slender blunted cones.

Esfahanian and Hejranfar [3] demonstrated that the PNS schemes can efficiently be used for providing basic flow models required for stability analysis of hypersonic axisymmetric laminar flows of the perfect gas over slender sharp and blunt cones. They used a combined TLNS-PNS solution procedure for the blunt cone case. This dual-code solution procedure has also been used to accurately and efficiently compute hypersonic laminar flows including real gas effects over long slender blunt bodies [6]. Both the TLNS and PNS equations were numerically solved by using the efficient implicit non-iterative finite-difference algorithm of Beam and Warming together with a shock fitting technique [3,6-9]. The numerical algorithms based on centrally differenced such as the Beam-Warming scheme in conjunction with a shock fitting procedure, can provide accurate and smooth solutions for geometries have small axial geometric variation.

The main objective of the present work is to accurately and efficiently compute hypersonic transitional/turbulent flows including equilibrium gas effects over long axisymmetric blunt bodies. In fact, for long slender blunt bodies at high Mach numbers, laminar flow at some distances becomes turbulent flow and flow solver has to be able to compute both flow regimes. The TLNS-PNS solution procedure used herein can be performed for both laminar and turbulent flows. The TLNS equations are solved in the nose region to provide the initial data plane needed for the solution of the PNS equations. Then, the PNS equations are employed to efficiently compute the flowfield for the afterbody region by using a space marching scheme.

For turbulent flow simulations, the two-layer eddy-viscosity turbulence models, namely the Cebeci-Smith (CS) [10] and the Baldwin-Lomax (BL) [11] models are employed. For the transitional region, the present scheme uses the model proposed by Dhawan and Narasimha (DN) [12]. In this model, continuous transition is affected by defining a streamwise transition intermittency factor that modifies the eddy viscosity over the transition region. Gupta et al. [13] have studied the application of both the CS and BL turbulence models to the solution of high speed flowfields over blunt bodies. They have used a viscous shock layer (VSL) solver for the case of perfect gas model. Herein, a combined TLNS-PNS solution procedure is used for both the perfect gas and the equilibrium air.

To demonstrate the accuracy and efficiency of using the present TLNS-PNS solution procedure, several computations are performed for hypersonic laminar and transitional/turbulent flows over blunt-body geometries. The results of these computations are compared with available numerical and experimental results and the effects of real gas on the flow variables are also studied.

2 Problem Formulation

The TLNS and PNS codes [3,6-8] were previously developed for computing hypersonic axisymmetric laminar flowfield for the perfect gas or the equilibrium air over blunt bodies. Here, these codes are extended to allow computations of transitional/turbulent flowfields.

2.1 The TLNS Equations

The TLNS equations are obtained from the compressible Navier-Stokes equations by neglecting the streamwise viscous and heat flux terms compared to the normal derivatives. The resulting equations for axisymmetric compressible flow can be written in dimensionless and conservation form in the general nonorthogonal curvilinear coordinate system (τ, ξ, η) as

$$\frac{\partial \bar{U}}{\partial \tau} + \frac{\partial \bar{F}}{\partial \xi} + \frac{\partial \bar{G}}{\partial \eta} + \bar{H} = 0$$
$$\bar{F} = \bar{F}_i, \quad \bar{G} = \bar{G}_i - \bar{G}_v, \quad \bar{H} = \bar{H}_i - \bar{H}_v \qquad (1)$$

where the solution vector is

$$\bar{U} = J^{-1}\tilde{U} = J^{-1}\left[\, \rho,\ \rho u,\ \rho v,\ E \right]^T$$

and $\bar{F}_i$, $\bar{G}_i$ and $\bar{H}_i$ are the inviscid flux vectors and $\bar{F}_v$, $\bar{G}_v$ and $\bar{H}_v$ are the viscous flux vectors.

2.2 The PNS Equations

The PNS equations are obtained by dropping the unsteady term in the TLNS equations and modifying the streamwise pressure gradient in the streamwise momentum equation to permit stable marching. The PNS equations for axisymmetric compressible flow in the generalized coordinate system (ξ, η) can be obtained from Eq. (1) as follows

$$\frac{\partial \bar{F}}{\partial \xi} + \frac{\partial \bar{G}}{\partial \eta} + \bar{H} = 0 \qquad (2)$$

The above equations have been nondimensionalized using the reference length R_N (dimensional nose radius) and freestream conditions.

To "close" the preceding system of equations, relations between the thermodynamic variables are required along with relations for the transport properties μ^* and k^*. For the present equilibrium flow computations, approximate curve fits are employed for thermodynamic and transport properties. The thermodynamic properties are obtained using the correlations developed by Sirinivasan et al. [14]

$$\begin{aligned} \gamma &= \gamma(\rho^*, e^*), & a^* &= a^*(\rho^*, e^*), \\ p^* &= p^*(\rho^*, e^*), & T^* &= T^*(\rho^*, e^*), \\ T^* &= T^*(\rho^*, p^*), & h^* &= h^*(\rho^*, p^*) \end{aligned} \qquad (3)$$

These curve fits are valid for temperatures up to 25000 K and density ratios (ρ^* / ρ_0^*) from 10^{-7} to 10^3. For both the equilibrium air and the perfect gas, the following relations between flow variables can be used

$$p = \rho e(\gamma - 1) \ , \ \gamma = \frac{h}{e} \ , \ E = \rho(e + \tfrac{1}{2}(u^2 + v^2))$$

The curve fits for the transport properties were developed by Srinivasan et al. [15] and include the following correlations

$$k^* = k^*(\rho^*, e^*) \quad , \quad \mu^* = \mu^*(\rho^*, e^*) \qquad (4)$$

These curve fits are valid for temperatures up to 15000 K and density ratios (ρ^* / ρ_0^*) from 10^{-5} to 10^1.

For perfect-gas computations, $\gamma = \gamma_\infty$, the molecular viscosity μ is determined by the Sutherland law and the coefficient of thermal conductivity is calculated by assuming a constant Prandtl number, $Pr = 0.72$.

The PNS equations are a mixed set of hyperbolic-parabolic equations in the marching direction, provided that the inviscid flow is supersonic, the streamwise velocity component is everywhere positive, and the streamwise pressure gradient term is either dropped in the subsonic regions or the "departure behavior" is

suppressed using a suitable technique. For this study, the Vigneron et al. [16] technique is implemented to prevent departure solutions.

In the Vigneron et al. approximation, the streamwise pressure gradient in the momentum equations is split into an implicit contribution and an explicit contribution

$$\frac{\partial p}{\partial \xi} = \left[\omega \frac{\partial p}{\partial \xi}\right]_{\text{implicit}} + \left[(1-\omega)\frac{\partial p}{\partial \xi}\right]_{\text{explicit}} \qquad (5)$$

The weighting function ω is determined as

$$\omega = \min\left[1, \frac{\sigma\gamma {M^2}_{\xi}}{1+(\gamma-1){M^2}_{\xi}}\right] \qquad (6)$$

where ${M}_{\xi}$ is the local streamwise Mach number and σ is a safety factor to account for nonlinearities in the analysis. To introduce the Vigneron et al. technique into the PNS equations, a new vector $\bar{F}^*$ is defined as

$$\bar{F}^* = \bar{F} - P \qquad (7)$$

Thus, the new form of the PNS equations appears as

$$\frac{\partial \bar{F}^*}{\partial \xi} + \frac{\partial P}{\partial \xi} + \frac{\partial \bar{G}}{\partial \eta} + \bar{H} = 0 \qquad (8)$$

where the inviscid vectors $\bar{F}^*$ and P are

$$\bar{F}^* = J^{-1}\begin{bmatrix} \rho U \\ \rho u U + \omega \xi_x p \\ \rho v U + \omega \xi_y p \\ (E+p)U \end{bmatrix}, \quad P = J^{-1}\begin{bmatrix} 0 \\ \xi_x(1-\omega)p \\ \xi_y(1-\omega)p \\ 0 \end{bmatrix}$$

and U denotes the contravariant velocity in the ξ direction, $U = \xi_x u + \xi_y v$. In the present PNS solver, the "elliptic" part of the streamwise pressure gradient term $(\partial P / \partial \xi)$ responsible for upstream disturbance propagation is omitted to permit the space-marching procedure to be stable.

3 Turbulence Models

Algebraic turbulence models are easily implemented and they require less computational efforts as compared to the one or two-equations models of turbulence. Two widely algebraic turbulence models, namely the Cebeci-Smith (CS) [10] and the Baldwin-Lomax (BL) [11] models are employed, in the present solution procedure, for turbulent flow simulations over long slender blunt bodies.

For turbulent-flow computations, a Reynolds averaged form of the TLNS and the PNS equations are used. Therefore, the dependent variables represent mean-flow contribution. By using the Boussinesq hypothesis, turbulence modeling is reduced to evaluate the turbulent viscosity coefficient μ_t. Consequently, the Reynolds average form of the TLNS and PNS equations can be obtained by replacing the laminar flow coefficients with

$$\mu = \mu_l + \mu_t \;, \quad \frac{\mu}{Pr} = \frac{\mu_l}{Pr_l} + \frac{\mu_t}{Pr_t} \qquad (9)$$

where the coefficient of viscosity μ_l is computed by Sutherland's law, Pr_l is assumed to be constant and equals to 0.72 and a value of 0.90 is used for Pr_t. The turbulent viscosity coefficient μ_t is calculated using the CS, BL and modified BL (MBL) turbulence models.

3.1 Cebeci-Smith Model

The CS turbulence model uses a two-layer eddy viscosity formulation (in dimensional form)

$$\begin{matrix} \text{if} \quad y \geq y_m \\ \text{if} \quad y > y_m \end{matrix} \quad \mu_t = \begin{cases} \mu_{ti} \\ \mu_{to} \end{cases} \qquad (10)$$

where y is the normal distance from the wall and y_m is the smallest value of y at which the value of μ_t from the inner and outer formulas are equal. The eddy viscosity in the inner region is defined by

$$\mu_{ti} = \rho l^2 |\Omega| \qquad (11)$$

where Ω is the magnitude of the vorticity and l is the Prandtl's mixing length

$$l = 0.4y\left[1 - \exp\left(-\frac{y}{A}\right)\right] \qquad (12)$$

The parameter A is usually referred to as the damping factor. The damping factor A is a strong function of the wall boundary conditions and is expressed as

$$A = 26\nu\left(\frac{\tau_{\mathrm{w}}}{\rho}\right)^{-\frac{1}{2}} \tag{13}$$

Eq. (12) was originally obtained for incompressible, zero pressure gradient ($p = \text{Constant}$, $dp/dx = 0$) and solid-wall flow ($u_{\mathrm{w}} = v_{\mathrm{w}} = 0$). However, this relation are applied to compressible flows where p and v are evaluated locally across the viscous sublayer region.

In CS turbulence model, the Prandtl's mixing length for compressible flow is defined as follows

$$l = 0.4y\left[1 - \exp\left(-(\frac{\nu_{\mathrm{w}}}{\bar{\nu}})^{\frac{1}{2}}\frac{y}{A}\right)\right] \tag{14}$$

where $\bar{\nu}$ is the average value of the kinematics viscosity taken over the viscous sublayer; $\bar{\nu} = \frac{1}{\mathrm{N_{sl}}}\sum_{\mathrm{i=1}}^{\mathrm{N_{sl}}}\nu_{\mathrm{i}}$. $\mathrm{N_{sl}}$ is the number of grid points in the viscous sublayer region. It should be noted that the density and the viscosity appearing in Eq. (13) are evaluated locally.

The eddy viscosity in the outer region can be expressed as follows

$$\mu_{to} = 0.0168\rho u_e \delta^*_{\mathrm{inc}} \mathrm{F_{kleb}}(y) \tag{15}$$

where δ^*_{inc} is the incompressible displacement thickness

$$\delta^*_{\mathrm{inc}} = \int_0^{y_e}(1 - \frac{u}{u_e})dy$$

and the Kelbanoff's intermitency function $\mathrm{F_{kleb}}(y)$ is defined by

$$\mathrm{F_{kleb}}(y) = \left[1 + 5.5\left(\frac{y}{\delta}\right)^6\right]^{-1}$$

The boundary-layer thickness is calculated using a total enthalpy model. In this model, it is assumed that an appropriate value for the boundary-layer thickness is equal to the value of the normal coordinate where

$$\frac{h_0 - h_w}{h_{0\infty} - h_w} = 0.995 \tag{16}$$

3.2 Original Baldwin-Lomax Turbulence Model

The BL turbulence model was initially developed based on the CS model with modifications that avoid the necessity for calculating the edge of the boundary layer. In the BL turbulence model, the eddy viscosity can be expressed by Eq. (10). This model employs a formulation similar to the CS model for the eddy viscosity in the inner region

$$\mu_{\mathrm{ti}} = \rho l^2 |\Omega| \tag{17}$$

where Ω is the magnitude of the vorticity and l is the Prandtl's mixing length

$$l = 0.41y\left[1 - \exp\left(-\frac{y^+}{26}\right)\right]$$

where y^+ is defined by

$$y^+ = \frac{\rho_{\mathrm{w}} u^* y}{\mu_{\mathrm{w}}} \quad , \quad u^* = \sqrt{\frac{\tau_{\mathrm{w}}}{\rho_{\mathrm{w}}}}$$

The eddy viscosity in the outer region of the viscous layer is based on the Kelbanoff expression

$$\mu_{\mathrm{to}} = 0.0269\rho \mathrm{F_{wake}} \mathrm{F_{kleb}}(\mathrm{y}) \tag{18}$$

where the Kelbanoff's intermitency function $\mathrm{F_{kleb}}(\mathrm{y})$ is defined by

$$\mathrm{F_{kleb}}(y) = \left[1 + 5.5\left(\frac{0.3y}{y_{\max}}\right)^6\right]^{-1}$$

and $\mathrm{F_{wake}}$ is

$$\mathrm{F_{wake}} = y_{\max}\mathrm{F_{max}}$$

The quantity $y_{\max}$ and $\mathrm{F_{max}}$ are determined from the function

$$\mathrm{F}(y) = y|\Omega|\left[1 - \exp\left(-\frac{y^+}{26}\right)\right]$$

The quantity F_{max} is the maximum value of $F(y)$ that occurs in a profile and y_{max} is the value of y at which it occurs.

The present calculations for hypersonic equilibrium flows over blunt bodies have indicated that the original BL turbulence model can not accurately predict the surface heating rates. Here, the BL turbulence model which does not require any calculation of the edge of the boundary layer is modified to improve the accuracy of the results.

3.3 Modified Baldwin-Lomax Turbulence Model

The original BL turbulence model was proposed for constant pressure boundary layer at transonic speeds. This model has been modified as discussed in Ref. [13] to include the effects of pressure gradient on the damping factor. This model employs a formulation similar to the CS model for the eddy viscosity in the inner region. The eddy viscosity in the inner region is defined by Eq. (11) and the Prandtl's mixing length l is given by Eq. (12) except that the damping constant is defined as

$$A = 26\left(\frac{\tau}{\tau_w}\right)^{-\frac{1}{2}} \tag{19}$$

τ is the local shear stress obtained from

$$\tau = (\mu_l + \mu_t)\Omega \tag{20}$$

In the outer region, the eddy viscosity is obtained similar to the original BL turbulence model. The eddy viscosity in the outer region is defined by Eq. (18) in which the damping factor A is determined by Eq. (19). This modification improves the accuracy of the results considerably.

3.4 Transition Region

For the transitional region, the present scheme uses the model proposed by DN [12]. In this model, continuous transition is affected by defining a streamwise transition intermittency factor (γ_{tr}) that modifies the eddy viscosity over the transition region ($x \geq x_{tr}$). In the transition region, the streamwise intermittency factor is evaluated using the following relation

$$\gamma_{tr} = \left[1 - \exp(-0.412\bar{x}^2)\right] \leq 1 \tag{21}$$

where

$$\bar{x} = \frac{2.96(x - x_{tr})}{x_{tr}} \tag{22}$$

Both continuous and instantaneous transition from laminar to turbulent flow are include in the present calculations.

4 Boundary Conditions and Initial Data Plane

The boundary conditions at the wall consist of no-slip conditions for velocity components ($u = v = 0$), a specified wall-temperature or an adiabatic wall, and zero pressure gradient approximation normal to the wall. For a perfect gas, the density at the wall is determined using the perfect gas relation. For a real gas, the wall density is calculated implicitly from the curve fit expression, $T = T(\rho^*, p^*)$. At the upper boundary, the bow shock is fitted using a shock fitting technique to obtain an accurate solution of both the TLNS and PNS equations near the shock.

The starting data of the PNS equations are provided by the solution of the TLNS equations in the nose region of the blunt-body configuration. The starting solution on an initial data surface where the inviscid flow is supersonic is obtained from the solution of the TLNS solution.

5 Computational Grid

An algebraic grid scheme is utilized to compute flowfield. The lines of constant ξ are distributed uniformly along the body surface and are orthogonal to the body. To insure that the viscous regions are adequately resolved, the lines of constant η are clustered near the body surface according to [17]

$$\frac{x-x_w}{x_s-x_w}=\bar{a},\quad \frac{x-x_w}{x_s-x_w}=\bar{a}$$
$$\bar{a}=1+\beta\left[\frac{1-\tilde{a}^{(1-\eta/\eta_{\max})}}{1+\tilde{a}^{(1-\eta/\eta_{\max})}}\right],\tilde{a}=\frac{\beta+1}{\beta-1} \tag{23}$$

in which the clustering parameter β is typically assigned in the range of 1.001-1.01.

6 Numerical Solution

The numerical solution of both the TLNS and PNS equations for equilibrium-air calculations is obtained by using the efficient implicit non-iterative finite difference algorithm of Beam and Warming together with a shock fitting procedure. Details of the derivations of the TLNS equations for equilibrium airflows and the numerical algorithm have been reported in Refs. [6,18]. The numerical algorithm for the PNS equations for a marching step $\Delta\xi$ can be written in delta form as

$$\left[\left[\frac{\partial\bar{F}^*}{\partial\bar{U}}\right]^i+\frac{\theta_1\Delta\xi}{1+\theta_2}\frac{\partial}{\partial\eta}\left[\left[\frac{\partial\bar{G}}{\partial\bar{U}}\right]^i+\left[\frac{\partial\bar{H}}{\partial\bar{U}}\right]^i\right]\right]\Delta\bar{U}^i=$$
$$-\frac{\Delta\xi}{1+\theta_2}\left[\frac{\partial\bar{G}}{\partial\eta}+\bar{H}\right]^i+\frac{\theta_2}{1+\theta_2}\Delta\bar{F}^{i-1}-\Delta P^i \tag{24}$$
$$-\Delta\xi\left[\frac{\partial\bar{F}^*}{\partial\xi}\right]^i_{\bar{U}}-\frac{\theta_1(\Delta\xi)^2}{1+\theta_2}\left[\frac{\partial}{\partial\eta}\left[\frac{\partial\bar{G}}{\partial\xi}\right]^i_{\bar{U},\bar{U}_\eta}+\left[\frac{\partial\bar{H}}{\partial\xi}\right]^i_{\bar{U},\bar{U}_\eta}\right]$$

where the derivative $\left[\partial/\partial\bar{U}\right]$ is referred to as Jacobian matrix and the subscripts $\bar{U}$ and $\bar{U}_\eta$ represent terms that are evaluated with $\bar{U}$ and $\bar{U}_\eta$ held fixed. The algorithm utilizes the first-order backward Euler implicit scheme $(\theta_1=1,\ \theta_2=0)$ in the marching direction ξ and the second-order central scheme in the normal direction η.

The inviscid and viscous flux vectors for a real gas can be written in the functional form of $\bar{U}$ and $\gamma=\gamma(\rho,e)$, For example, the flux vector $\bar{F}^*$ is expressed as $\bar{F}^*(\bar{U},\gamma)$ and therefore the Jacobian matrix A^* of the flux vector $\bar{F}^*$ is given by [19,20]

$$A^*=\left[\frac{\partial\bar{F}^*}{\partial\bar{U}}\right]_\gamma+J\left[\frac{\partial\bar{F}^*}{\partial\gamma}\right]_{\bar{U}}$$
$$\left\{\rho_\infty\left[\frac{\partial\gamma}{\partial\rho^*}\right]_{e^*}\left[\frac{\partial\rho}{\partial\tilde{U}}\right]+\frac{a_\infty^2}{\gamma_\infty}\left[\frac{\partial\gamma}{\partial e^*}\right]_{\rho^*}\left[\frac{\partial e}{\partial\tilde{U}}\right]\right\} \tag{25}$$

For a real gas, the derivatives ($\left[\partial\gamma/\partial e^*\right]_{\rho^*}$) and ($\left[\partial\gamma/\partial\rho^*\right]_{e^*}$) can be computed directly from curve fit expression $\gamma=\gamma(\rho^*,e^*)$.

The preceding system of equations along with the boundary conditions at the wall and the shock gives a block tridiagonal system of equations for $\Delta\bar{U}^i$ with a block size of 4×4. A block-tridiagonal solver is used to calculate the incremental solution vector $\Delta\bar{U}^i$, and then the solution vector is determined as follows

$$\bar{U}^{i+1}=\bar{U}^i+\Delta\bar{U}^i \tag{26}$$

High-order dissipation terms must be added to this scheme in order to damp high frequency oscillations associated with the central differencing of derivatives in the η-direction. Therefore, second-order implicit and fourth-order explicit dissipation terms of the form

$$D_i=-\varepsilon_i J^{-1}\left(\nabla_\eta\Delta_\eta\right)J\left[\frac{\partial\bar{F}^*}{\partial U}\right]^i\Delta\bar{U}^i,\ \varepsilon_i=2\varepsilon_e$$
$$D_e=-\varepsilon_e\left[\frac{\partial\bar{F}^*}{\partial U}\right]^i J^{-1}\left(\nabla_\eta\Delta_\eta\right)^2 J\bar{U}^i,\ \varepsilon_e<\frac{1}{8} \tag{27}$$

are added to the left and right-hand sides of Eq. (24). The explicit and implicit dissipation coefficients are set to $\varepsilon_e=0.01$ and $\varepsilon_i=2\varepsilon_e$.

6.1 Shock Fitting Procedure

For the PNS solution, at each station, the shock slope is iteratively corrected in an explicit manner and the flow properties behind the shock are computed by using the compatibility and Rankine-Hugoniot relations. The pressure behind the shock for the equilibrium-air computation is determined by integrating the energy equation in the non-conservative form as follows

$$U\frac{\partial p}{\partial \xi}+V\frac{\partial p}{\partial \eta}-\frac{p}{\gamma-1}\left[U\frac{\partial \gamma}{\partial \xi}+V\frac{\partial \gamma}{\partial \eta}\right]+ \gamma p\left[\xi_x\frac{\partial u}{\partial \xi}+\xi_y\frac{\partial v}{\partial \xi}+\eta_x\frac{\partial u}{\partial \eta}+\eta_y\frac{\partial v}{\partial \eta}+\frac{v}{y}\right]=0 \quad (28)$$

The iterative process is repeated at the shock until the solution converges and then the solution marches on the next solution plane.

7 Numerical Results

The present TLNS-PNS solution strategy is used to accurately and efficiently compute high Mach number transitional/turbulent flows of perfect gas and equilibrium air over blunt-body configurations. The results of these computations are compared with available numerical and experimental results and the effects of real gas on the flow variables are also studied.

7.1 Laminar Flow

The first test case is hypersonic laminar flow of equilibrium air over a long slender blunted cone. The flow conditions for this test case correspond to the Reentry-F flight altitude of 120,000 ft [21]. The Reentry-F configuration is a 5-deg half angle sphere-cone and an overall length of 13 ft with an initial nose radius of $R_N = 0.114$ in. The flow conditions are

$M_\infty = 19.25$, $Re_\infty = 7670.4$,
$p_\infty = 768.27\,\mathrm{Pa}$, $T_\infty = 243\ \mathrm{K}$,
$\rho_\infty = 67.144\times10^{-5}\ \mathrm{kg.m^{-3}}$, $T_w = 477.77\text{-}361.11\mathrm{K}$

This is a challenging case to compute high Mach number over such a large scale model. The present TLNS-PNS approach is applied to this case to show the efficiency and accuracy of the proposed method [6].

The TLNS solution in the nose region ($S \le 3.0$) is obtained by using the grid points $(30,100)$ in (ξ,η) directions, respectively, to provide the initial data for the PNS solver. The PNS solution is obtained by using the stepsize $\Delta S = 0.1$ in the marching direction and the wall-normal grid points $\mathrm{Jmax} = 100$ and the stretching parameter $\beta = 1.005$. Figure 1 indicates the computed flowfield for the Mach number contours for the region $S \le 6.0$. This figure also shows the initial conditions and the marching procedure for the PNS equations.

Figure 2 demonstrates the effect of grid refinement on the surface heating rates for the equilibrium airflow. It is found that the surface heating rate is more sensitive to the number of grid points and grid distribution used, especially for the afterbody region of long blunt-body configurations. The study shows that the clustering of the grid near the wall can improve accuracy of the results computed with a lower number of grid points. The numerical results suggest that $J_{\max} = 100$ and $\beta = 1.005$ are sufficient for the computations even for the downstream of the flowfield.

Figure 3 compares the computed surface heating rates from the present technique with the experimental Reentry-F flight data, the VSL solution [22] and also the results of Bhutta and Lewis [23] obtained using a PNS scheme. The PNS solution by Bhutta and Lewis was obtained by the initial data surface from a VSL solution in the nose region. The Reentry-F flight experiment involved the accurate measurement of surface heating rates on long slender conical RV under laminar flow conditions. The results of the present solution are found to be in good agreement with the experimental data and those of Bhutta and Lewis. The study shows the VSL method underpredicts the surface heating rates especially near the pressure overexpansion/recompression region. This may be because the VSL solution scheme is very sensitive to the accuracy of the input shock shape data for long slender configurations. It can be seen that the surface heating rates for the perfect gas is lower than that of the equilibrium case.

For the equilibrium airflow computation, the typical CPU time of the PNS solution, using 200 grid points in the wall-normal direction and 15000 sweeps in the streamwise direction, is 5 min and the CPU time of the TLNS solution in the nose region using (30,100) grid points is about 1 h (on a personal computer). It is clear that the present TLNS-PNS solution strategy

significantly reduces the computer time and storage required to obtain the equilibrium flowfield with reasonable accuracy.

7.2 Transition/Turbulent Flow

7.2.1 Perfect Gas

The present computations are performed for hypersonic transitional/turbulent flow of perfect gas over a long slender blunted cone with 5° half angle. The nose radius is $R_N = 1.5$ in. and the solution is computed for a body length of $S = 1200$. The flow conditions are:

$$M_\infty = 15, \qquad Re_\infty = 19210.887,$$
$$p_\infty = 130.4488\,\text{Pa}, \qquad T_\infty = 265.556\ \text{K},$$
$$\rho_\infty = 171.16 \times 10^{-5}\ \text{kg.m}^{-3}, \qquad T_w = 1255.556\,\text{K}$$

In this case, the TLNS-PNS solution procedure is also employed. The TLNS solution in the nose region ($S \le 3.85$) is obtained by using the grid points $(40,100)$ in (ξ, η) directions, respectively. Then the PNS solution is performed by using the stepsize $\Delta S = 0.1$ in the marching direction and $\text{Jmax} = 100$ and $\beta = 1.001$.

For this case, both laminar and transitional/turbulent flows are studied. For the turbulent flow the CS turbulence model is used and the DN model is applied in the transition region in which the transition point occurs at $S = 192$. Figure 4 indicates the computed surface heating rates of the perfect gas for the different number of grid points. It is found that $\text{Jmax} = 100$ with the stretching factor $\beta = 1.001$ is adequate.

In Fig. 5, the computed surface heating rates for laminar and transitional/turbulent flows are compared with the VSL results [13]. For the laminar flow, the computed surface heating rates and the VSL results are in geed agreement. To simulate the turbulent flow, both the CS and BL turbulence models are employed. It is found that the calculated results of the CS model are in good agreement with the VSL results, but the original BL model overpredicts the surface heating rates in the turbulent region by approximately 23%. The original BL turbulence model is obtained for constant pressure boundary layers. In this study, the BL model is modified to include the effect of pressure gradient on the damping factor. As shown in this figure, the results of this modification indicate significant improvement in comparison with the CS results.

For computing the eddy viscosity, the CS model uses the enthalpy gradient (Eq. 16) to determine the boundary layer edge. The effect of definition of boundary layer edge on the surface heating rates is shown in Fig. 6. It is found that the results based on the CS model are very sensitive to the definition of the boundary layer edge. It should be noted that the BL model computes the eddy viscosity without the necessity of determining the edge of boundary layer, and therefore, the modified BL turbulence model is preferable than the CS model for computing hypersonic equilibrium turbulent flows.

7.2.2 Equilibrium Gas

The third test case is hypersonic transitional/turbulent flow of equilibrium air over a long slender blunted cone with a total length of $x^* / R_N = 1500$. The flow conditions for this test case correspond to the Reentry-F flight altitude of 80,000 ft. [21]. The Reentry-F configuration is a 5-deg half angle sphere-cone with an initial nose radius of $R_N = 1.4$ in. The flow conditions are

$$M_\infty = 19.97, \qquad Re_\infty = 65898.745,$$
$$p_\infty = 2803.868\,\text{Pa}, \qquad T_\infty = 219.5\,\text{K},$$
$$\rho_\infty = 4447136 \times 10^{-5}\ \text{kg.m}^{-3}, \qquad T_w = 430.5 - 603.33\text{K}$$

The grid size and the grid distribution for the solution of the TLNS code in the nose region are similar to the previous test case. In the transition region, both the instantaneous transition and the DN model are applied to fully turbulent conditions. For instantaneous transition, the transition point occurs at location of $x^* / R_N = 7550$ and for the DN model occurs at $x^* / R_N = 6000$.

The effect of grid refinement on the results of surface heating rates is shown in Fig. 7. These results are computed using the modified

BL model in the turbulent region. The results show no difference between the 100 and 200 grid points in the normal direction, whereas 50 grid points predict inadequate results. For the CS turbulence model, the effect of definition of boundary layer edge on the surface heating rates is shown in Fig. 8. It is found that the results are very sensitive to definition of boundary layer edge based on enthalpy gradient (Eq. 16). Therefore, in the CS model, selecting a regular value for the enthalpy gradient is relatively difficult and finer resolution and accurate solutions near the edge of boundary layer are essential.

The present computations for the surface heating rates for the equilibrium airflow based on the CS, BL and modified BL (MBL) turbulence models are compared with the experimental data [21] and the Bhutta and Lewis results [23] as shown in Figs. 9 and 10. The present results in Fig. 9 are computed with instantaneous transition whereas Fig. 10 indicates the results using the DN transition model in the transition region. The calculated results of the CS turbulence model are in good agreement with the experimental data and the Bhutta results, but the original BL turbulence model overpredicts the results in the turbulent region by approximately 36% without using the transition model and 25% with using the DN transition model. It is obvious, with the modification in the BL formulation, similar to the perfect gas case, the results of equilibrium air are extremely improved and corresponded with the experimental data. The BL and CS turbulence models have been studied by Gupta et al. [13] only for the perfect gas. In the present study both the equilibrium air and the perfect gas are considered.

Figure 11 demonstrates the velocity profiles of the equilibrium airflow for the BL, CS and MBL models at the station $x^*/R_N = 1200$ where the flow is fully turbulent. The results indicate that the velocity profiles using the MBL and CS turbulence models are nearly the same, and the original BL model can not accurately predict the velocity profile.

To investigate the real gas effects, a comparison of the surface heating rates for the perfect gas and the equilibrium air with the experimental results is shown in Fig. 12. The results indicate that the perfect gas model underpredicts the surface heating rates by approximately 7% in the laminar region and 18% in the turbulent region.

8 Concluding Remarks

A combined TLNS-PNS solution procedure has been implemented to accurately and efficiently compute hypersonic laminar and transition/turbulent flowfields over blunt-body configurations. Both the TLNS and PNS schemes have been solved by using the efficient implicit non-iterative finite-difference algorithm of Beam and Warming in conjunction with a shock fitting procedure.

For turbulent flows, two algebraic turbulence models, namely, the Cebeci-Smith (CS) and the Baldwin-Lomax (BL) models have been used for application to the hypersonic equilibrium air flows over long slender blunt bodies. The CS model is sensitive to the definition of the edge of boundary layer and requires finer resolution near the edge. The BL model, that does not require the determination of the boundary-layer thickness, has been corrected and applied successfully to the hypersonic equilibrium flows. Both of the CS and modified BL (MBL) turbulence models are shown to result in similar heating predictions for hypersonic equilibrium airflows over long blunt bodies.

The grid refinement study shows the wall heating rates especially for long blunt-body geometry are sensitive to the number of grid points and the grid distribution used. The wall heating rates in laminar and turbulent region for the equilibrium airflow are higher than those of the perfect gas case.

The results of present computations of hypersonic flows over long blunt bodies are found to be in excellent agreement with available data. The present solution strategy significantly reduces the computational time and

memory required for computations of hypersonic equilibrium transitional/turbulent flows over long blunt-body geometries.

References

[1] Wood, W. A. and Eberhardt, S., "Dual-Code Solution Strategy for Chemically-Reacting Hypersonic Flows," AIAA Paper, 95-0158, 1995

[2] Wood, W. A., Thompson, R. A., and Eberhardt, S., "Dual-Code Solution Strategy for Hypersonic Flows," Journal of Spacecraft and Rockets, Vol. 33, No. 3, Dec. 1995, pp. 449-451

[3] Esfahanian, V., Hejranfar, K., "Accuracy of Parabolized Navier-Stokes Schemes for Stability Analysis of Hypersonic Axisymmetric Flows," AIAA Journal, Vol. 40, No. 7, 2002, pp. 1311, 1322.

[4] Gnoffo, P. A., Gupta, R. N., and Shinn, J. L., "Conservation Equations and Physical Models for Hypersonic Air Flows in Thermal and Chemical Nonequilibrium," NASA TP 2867, Feb. 1989.

[5] Buelow, P. E., Tannehill, J. C., Ievalts, J. O., and Lawrence, S. L., "Three-Dimensional, Upwind, Parabolized Navier-Stokes Code for Chemically Reacting Flows," Journal of Thermophysics and Heat Transfer, Vol. 5, No. 3, 1991, pp. 274-283.

[6] Hejranfar, K., Esfahanian, V., and Kamali-Moghadam, R., "Computation of Hypersonic Axisymmetric Flows of Equilibrium Gas over Blunt Bodies," *The 13th Annual Conference of the Computational Fluid Dynamics Society of Canada (CFD 2005),* Newfoundland, Canada, Aug. 2005.

[7] Esfahanian, V., "Computation and Stability Analysis of Laminar Flow over a Blunted Cone in Hypersonic Flow," Ph.D. Thesis, The Ohio State University, Columbus, Ohio, March 1991.

[8] Hejranfar, K., "Computation and Stability Analysis of Hypersonic Axisymmetric Flows Using Parabolized Schemes," Ph.D. Dissertation, Dept. of Mechanical Engineering, The University of Tehran, March 2002.

[9] Beam, R. M. and Warming R. F., "An Implicit Factored Scheme for the Compressible Navier-Stokes Equations," AIAA Journal, Vol. 16, No. 4, pp. 393-402, 1978.

[10] Cebeci, T., and Smith, A. M. O., "Analysis of Turbulent Boundary Layers," Academic, New York, 1974.

[11] Baldwin, B. S. and Lomax, H., "Thin-Layer Approximation and Algebraic Model for Separated Turbulent Flow," AIAA Paper 78-257, 16th Aerospace Sciences Meeting, Huntsville, Alabama, Jan. 1978.

[12] Dhawan, S., and Narasimha, R., "Some Properties of Boundary Layer Flow During the Transition Form Laminar to Turbulent Motion," *Journal of Fluid Mechanics,* Vol. 3, Jan. 1958, pp. 418-436.

[13] Gupta, R. N., Lee, K. P., Zoby, E. V., Moss, J. N., and Thompson, R. A., "Hypersonic Viscous Shock-Layer Solutions over Long Slender Bodies-Part I: High Reynolds Number Flows," *Journal of Spacecraft and Rockets,* Vol. 27, No. 2, 1990, pp. 175-184.

[14] Srinivasan, S., Tannehill, J. C. and Weilmuenster, K. J., "Simplified Curve Fits for the Thermodynamic Properties of Equilibrium Air," NASA RP-1-313, 1986.

[15] Srinivasan, S., Tannehill, J. C. and Weilmuenster, K. J., "Simplified Curve Fits for the Transport Properties of Equilibrium Air," NASA RP-1181, 1987.

[16] Vigneron, Y. C., Rakich, J. V., and Tannehill, J. C., "Calculation of Supersonic Viscous Flow over Delta Wings with Sharp Subsonic Leading Edges," AIAA paper 78-1137, July 1978.

[17] Tannehill, J. C., Anderson, D. A., and Pletcher, R. H., Computational Fluid Mechanics and Heat Transfer, 2nd ed., Taylor and Francis, Washington, DC., 1997.

[18] Hejranfar, K., Esfahanian, V., and Kamali-Moghadam, R., "Numerical Solution of Hypersonic Axisymmetric Flows over Blunt Noses including Equilibrium Gas Effects," *Proceedings of the 9th Fluid Dynamics Conference,* Shiraz, Iran, March 2004.

[19] Tannehill, J. C., Ievalts, J. O. and Lawrence, S. L. "An Upwind Parabolized Navier-Stokes Code for Real Gas Flows," AIAA Paper, 88-0713, 1988.

[20] Tannehill, J. C., Buelow, P. E., Ievalts, J. O., and Lawrence S. L., "Three-Dimensional Upwind Parabolized Navier-Stokes Code for Real Gas Flows," *Journal of Spacecraft and Rockets,* Vol. 27, No. 2, Aug. 1989, pp. 150-159.

[21] Stainback, P.C., Johnson, C. B., Boney, L. B., and Wicker, K. C., "Comparison of Theoretical Predictions and Heat-Transfer Measurements for a Flight Experiment at Mach 20 (Reentry F), ". NASA TM-X 2560, 1972.

[22] Thompson, R. A., Zoby, E. V., Wurster, K. E., and Gnoffo, P. A., "An Aerothermodynamic Study of Slender Conical Vehicles,". AIAA Paper 87-1475, June 1987.

[23] Bhutta, B. A., and Lewis, C. H., "Comparison of Hypersonic Experiments and PNS Predictions: Part I: Aerothermodynamics," *Journal of Spacecraft and Rockets,* Vol. 28, No. 4, 1990.

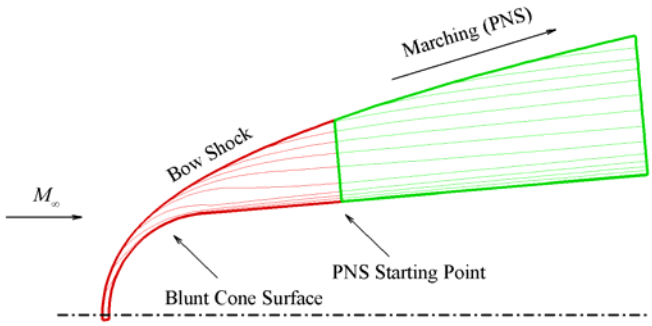

Fig. 1 Computed Mach contours and solution strategy for hypersonic laminar flow of equilibrium air over 5^0 sphere-cone, $M_\infty = 19.25$.

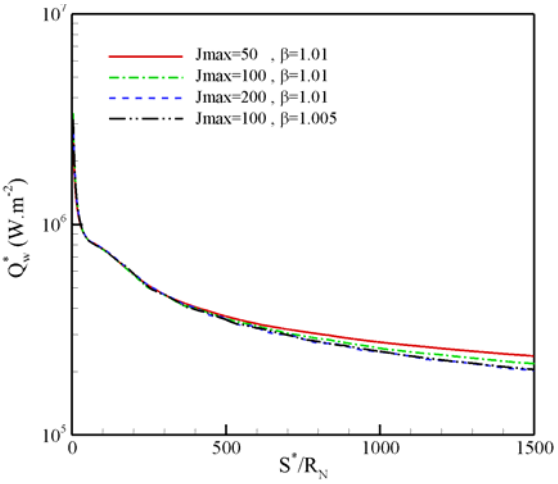

Fig. 2 Grid refinement study on surface heating rates for hypersonic laminar flow of equilibrium air over 5^0 sphere-cone, $M_\infty = 19.25$

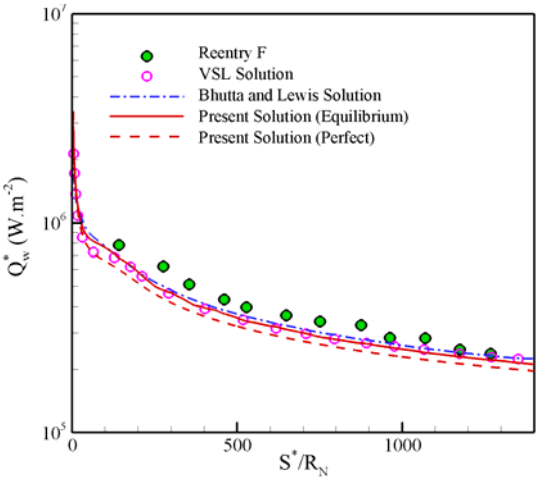

Fig. 3 Comparison of surface heating rates for hypersonic laminar flow of equilibrium air over 5^0 sphere-cone, $M_\infty = 19.25$

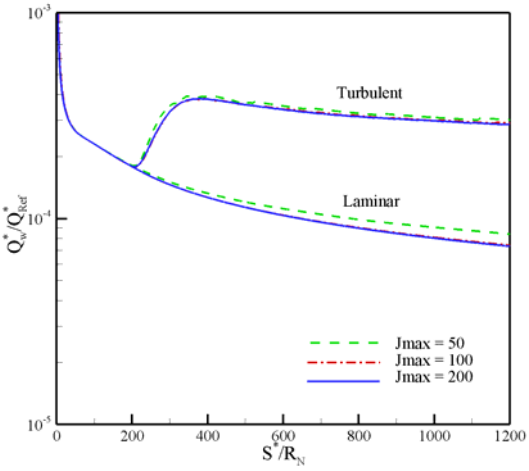

Fig. 4 Grid refinement study on surface heating rates for transitional/turbulent flow of perfect gas over 5^0 sphere-cone, $M_\infty = 15$

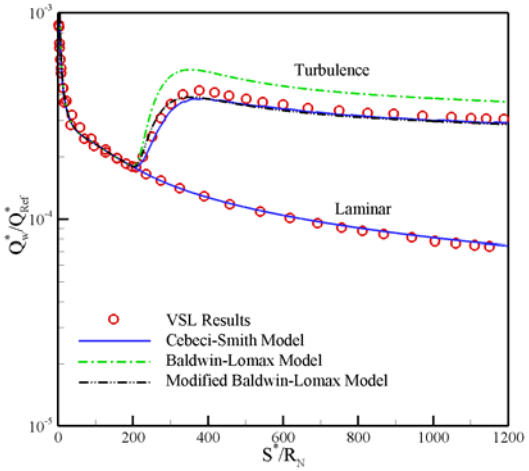

Fig. 5 Comparison of surface heating rates for transitional/turbulent flow of perfect gas over 5^0 sphere-cone, $M_\infty = 15$.

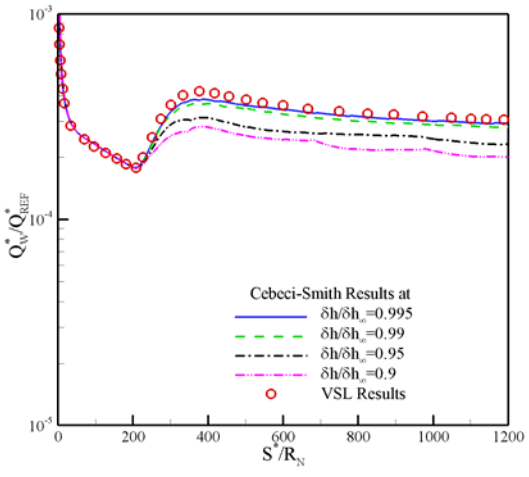

Fig. 6 Effect of definition of boundary layer edge on surface heating rates for transitional/turbulent flow of perfect gas over 5^0 sphere-cone, $M_\infty = 15$.

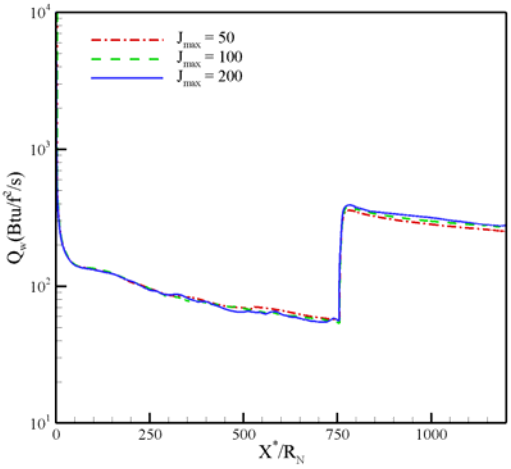

Fig. 7 Grid refinement study on surface heating rates for transitional/turbulent flow of equilibrium air over 5^0 sphere-cone, $M_\infty = 19.97$

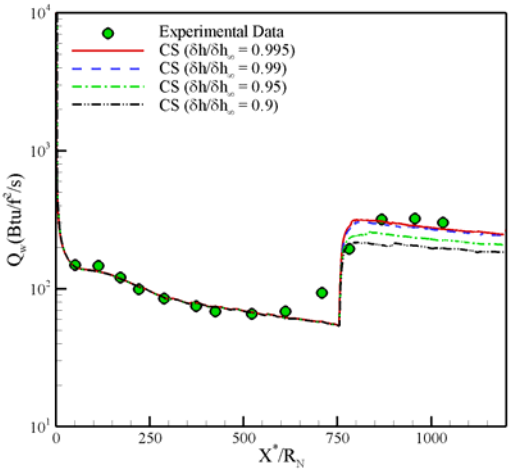

Fig. 8 Effect of definition of boundary layer edge on surface heating rates for transitional/turbulent flow of equilibrium air over 5^0 sphere-cone, $M_\infty = 19.97$

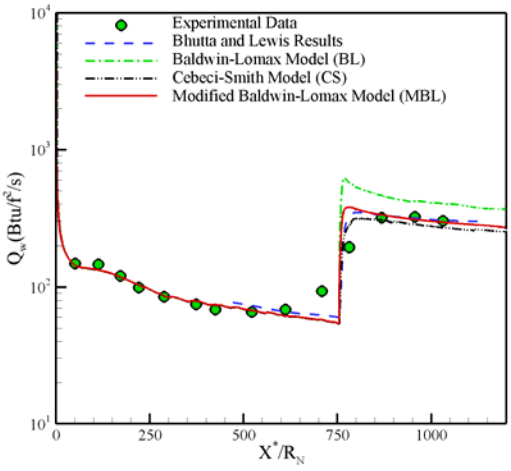

Fig. 9 Comparison of surface heating rates for transitional/turbulent flow of equilibrium air over 5^0 sphere-cone, $M_\infty = 19.97$.

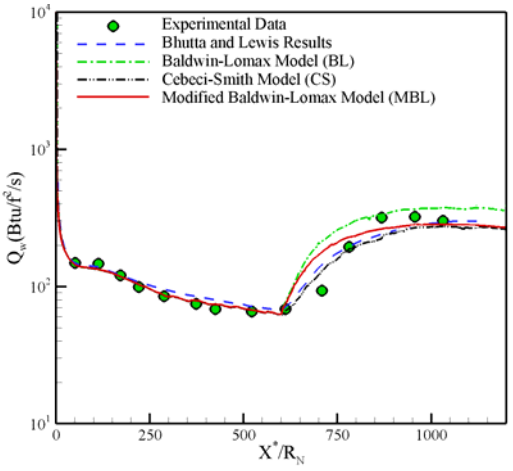

Fig. 10 Comparison of surface heating rates for transitional/turbulent flow of equilibrium air over 5^0 sphere-cone, $M_\infty = 19.97$

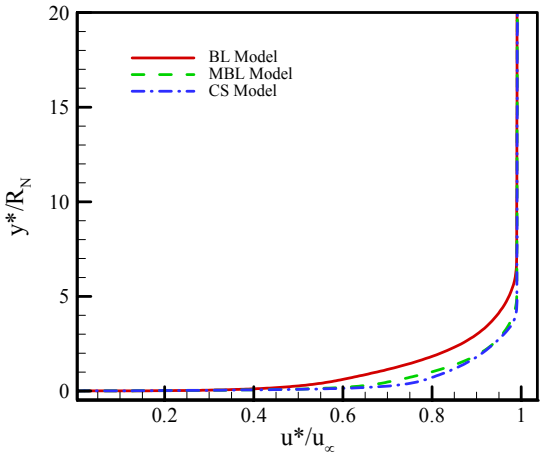

Fig. 11 Comparison of velocity profiles at $x^* / R_N = 1200$ for transitional/turbulent flow of equilibrium air over 5^0 sphere-cone, $M_\infty = 19.97$

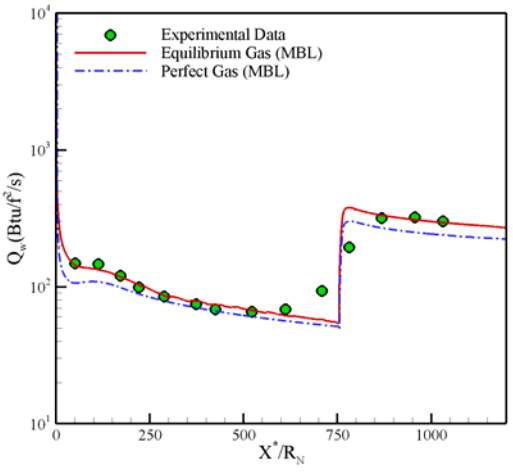

Fig. 12 Effect of real gas on surface heating rates for transitional/turbulent flow over 5^0 sphere-cone, $M_\infty = 19.97$